Practical Aspects of Rotor Cage Fault Detection for Medium-Voltage Induction Motors

Bin Lu
Senior Member, IEEE
Eaton Corporation
Bldg. 3, No. 280 Lin Hong Rd
Shanghai 200335 China
BinLu@Eaton.com

Zhi Gao
Senior Member, IEEE
Eaton Corporation
1000 Cherrington Pkwy
Moon Twp, PA 15108 USA
GeorgeGao@Eaton.com

Joel Benzing
Senior Member, IEEE
Eaton Corporation
211 Heywood Rd
Arden, NC 28704 USA
JoelEBenzing@Eaton.com

***Abstract* -- Predictive diagnostics offering early failure detection of large induction motors applied in metals, pulp & paper and other process industries are becoming increasingly important. As motors grow larger, industry has become increasingly reliant on technologies to detect rotor faults via on-line prognostics and arrange optimal maintenance intervals to increase productivity. Traditional broken rotor bar fault detection algorithms have historically relied largely on monitoring changes in the stator current spectra. This often results in nuisance warnings when the motor operates at different load levels, or when baseline data at healthy motor operations are not available. To address this issue, a fault severity evaluation technique is introduced in this paper to detect rotor cage failures using only current and voltage measurements, plus selected motor nameplate data and motor's geometric dimensions. The fault severity index can indicate the possibility of a rotor cage fault even in the absence of baseline data. This guarantees the algorithm's reliability in practical applications. In addition, a decision-making system, including an adaptive filter and fuzzy logic, is proposed to warn the user in the case of a rotor cage failure. Experimental results show that the proposed fault severity evaluation algorithm can reliably reflect the rotor cage status under different operating conditions, which can be further applied in the detection of rotor cage failures.**

***Index Terms*-- Induction motor, mechanical stress, medium-voltage motor, metal industries, process industries, rotor cage fault, thermal stress.**

I. INTRODUCTION

Large medium-voltage motors up to 8000 horsepower are widely used in process industries to drive various critical processes [1]-[4]. In process industry applications such as the metals industry, induction motors used in rolling mills, main mill stands and coiler reels often have cage-type rotor bars constructed with reinforced end rings to allow for increased strength and rigidity under different rolling conditions.

In rolling mill applications, large medium-voltage motors are often operated under environmental and mechanical stresses, such as high ambient temperature and water mist, rolling oil and emulsion in mill atmosphere. Similarly, large motors applied in applications such as paper machine vacuum pumps and thermo-mechanical pulping motors are critical loads in the papermaking process and are subjected to vibration, large temperature variations and frequent wash-down. Such environmental and mechanical stresses could lead to motor degradation and malfunction over the long run. The monitoring and protection of such medium-voltage induction motors is an essential element in the overall industrial processes protection scheme to avoid financial losses caused by unexpected process downtime [5].

Among various factors that cause motor failures, rotor cage fault is one of the most common faults of large medium-voltage motors [6]-[11]. Fig. 1 shows the distribution of typical induction motor failed components based on field investigations [9]-[10].

Compared to their low-voltage counterparts, medium-voltage motors are often rotor-limited rather than stator-limited, i.e., due to the high thermal stresses imposed on the rotor structure, a large medium-voltage motor may only be started a few times each hour, which is often much less than their smaller low-voltage counterparts. In addition, a large medium-voltage induction motor has a relatively lower margin in cooling capacity. This often leads to higher thermal stress in both rotor conductors and stator windings at the time when the motor is started.

The thermal stress during motor starts and at running overload conditions is a major cause of broken rotor bar/end-ring faults in medium-voltage induction motors [12]. The excessive overheating of the rotor cage causes thermal expansion and thus mechanical stresses on the rotor cage structure. Other major causes of rotor cage faults include [13], [14]:

1. Magnetic stresses caused by electromagnetic forces, unbalanced magnetic pull.
2. Dynamic stresses due to shaft torques.
3. Environmental stresses due to contamination, abrasion of rotor material.
4. Mechanical stresses due to loose laminations.

As shown in Fig. 1, along with other major motor faults, the broken-rotor-bar-induced motor malfunctions lead to high repair costs and significant financial losses due to unexpected facility downtime. Therefore, reliable monitoring and protection of medium-voltage motors afford process industries and their asset holders significant economic benefits.

Traditional rotor cage fault detection algorithms rely

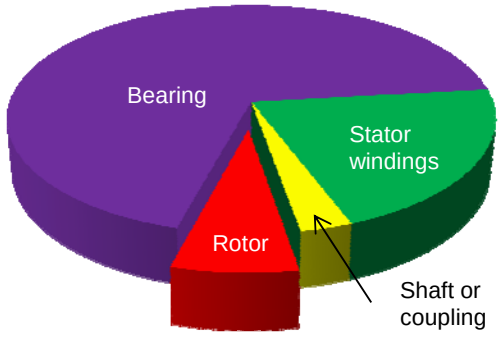

Fig. 1. Distribution of failed components in induction motors [10].

largely on the monitoring of changes in the stator current spectra, and may result in nuisance warnings when motor operates at different load levels. Those algorithms may also have difficulty detecting impending rotor cage fault when baseline data at healthy motor operations are not available.

To address the issue of timely detection of rotor cage faults, practical aspects of designing and implementing a broken rotor bar detection algorithm based on a ratio between the broken-rotor-bar-induced stator current harmonics and the rotor current must be addressed. The algorithm is also proposed with an aim to address the load-dependency issue that has been found in many prior rotor cage fault detection algorithm.

Section II below provides general background information on the broken rotor bar detection using the motor current signature analysis. Section III discusses a fault-severity-based approach to detect cage fault for medium-voltage induction motors. Practical considerations are further elaborated in Section IV, with experimental results given in Section V. Finally, conclusions are offered in Section VI.

II. Broken Rotor Bar Detection – Current Signature Analysis

For a large medium-voltage induction motor, a broken rotor bar or a loose connection between one of the rotor cage bars and an end-ring prevents the rotor current from flowing through the broken rotor bar or into the end ring. As shown in Fig. 2, a broken rotor bar along the *d*-axis causes an unbalance in the induced rotor current, and hence an unbalance in the rotor flux.

A. Broken-Rotor-Bar-Induced Stator Current Harmonics

The unbalanced rotor flux in this case can be decomposed into a positive and a negative sequence component, both of which are shown in Fig. 2, rotating at a slip frequency in opposite directions. The negative sequence rotor flux then produces counter-electromotive force, i.e., back-emf, in the stator and leads to a stator current harmonic. The overall current harmonics can be observed at twice the slip frequency beside the input frequency, as given in [15]-[17].

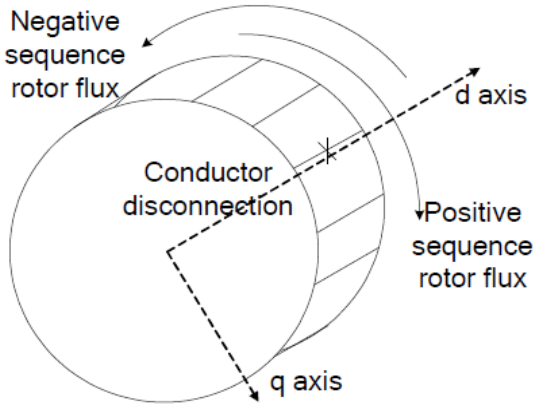

Fig. 2. Rotor cage fault and induced rotor flux unbalance.

$$f_b = (1 \pm 2ks) \cdot f_0 \tag{1}$$

where f_b is the frequency of the current related to broken rotor bar/end-ring fault; s is the slip; f_0 is the input frequency. The typical spectrum of stator current is shown in Fig. 3.

B. Speed Ripple

In Fig. 3, the fundamental current component is located at f_0, and the first sideband to the left of fundamental current component is

$$f_b = I_1 \cdot \cos[\,(1-2s)\omega t\,] \tag{2}$$

where $\omega = 2\pi f_0$.

This left sideband current harmonic interacts with the air-gap flux and produces an oscillatory torque ΔT

$$\Delta T = 3p\Psi \cdot I_1 \cdot \sin(\,2s\omega t\,). \tag{3}$$

where p is the motor's number of pole-pairs, and Ψ is the amplitude of the rotor flux.

Assuming a linear mechanical system, the oscillatory torque ΔT leads to speed ripples in the motor shaft

$$\Delta\omega = \int \frac{\Delta T}{J} dt = -\frac{3p\Psi}{2s\omega J} I_l \cos(2s\omega t) \tag{4}$$

where J is the motor-load's overall inertia.

C. Flux Linkage Phase Modulation

According to (4), the speed-ripple-induced motor shaft angular variation is

$$\Delta\theta = \int \Delta\omega dt = -\frac{3p\Psi}{4s^2\omega^2 J} I_l \sin(2s\omega t) \tag{5}$$

The angular variations of the motor shaft produce a phase modulation in the flux linkage

$$\begin{aligned} \Psi(t) &= \Psi \exp\left[j(\omega t - \Delta\theta)\right] = \Psi \exp(j\omega t) \\ &+ \frac{\Psi}{2} \frac{3p\Psi}{4s^2\omega^2 J} I_l \exp\left[j(1+2s)\omega t\right] \\ &- \frac{\Psi}{2} \frac{3p\Psi}{4s^2\omega^2 J} I_l \exp\left[j(1-2s)\omega t\right] \end{aligned} \tag{6}$$

where exp(·) designates an exponential function. The

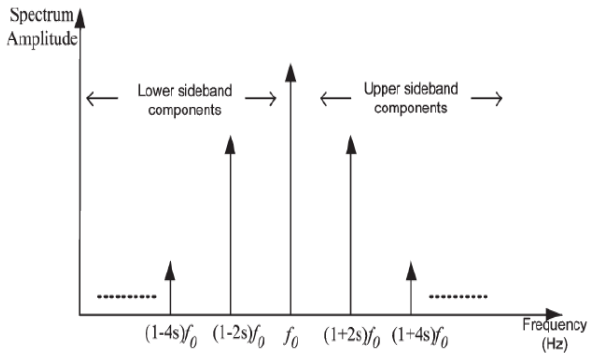

Fig. 3. Broken-rotor-bar-induced stator current harmonics.

positive sequence flux Ψ_p refers to the second term on the right side of (6), while the negative sequence flux Ψ_n refers to the third term on the right side of (6).

III. Broken Rotor Bar Detection – Fault Severity Analysis

When one bar is broken along the *d*-axis on a rotor cage with a total of *N* bars, as shown in Fig. 2, the positive and negative sequence fluxes have the following relationship

$$\frac{\Psi_n}{\Psi_p} = \frac{1}{N-1}. \tag{7}$$

Because the number of rotor bars is a fixed quantity for a given motor, the ratio between negative and positive sequence fluxes provides a good index that indicates the fault severity in the motor.

In practice, it is often difficult to measure the positive and negative sequence fluxes directly. Therefore, the fault severity has to be determined based some other measurable quantities, such as specific harmonics in the stator current. This section formulates such a fault severity index based on the relationship between the fluxes and current harmonics.

A. Motor Equivalent Circuit at $(1-2s)\cdot f_0$

Fig. 4 shows an equivalent circuit of the motor at $(1-2s)\cdot f_0$. The rotor current $I_{r,(1-2s)f}$, which is correlated with the negative sequence flux, operates like a current source in Fig. 4.

For most induction motors, the magnetizing impedance Z_m is usually much larger than the stator impedance Z_1. Consequently, the stator current is often regarded as the same as the rotor current at $(1-2s)\cdot f_0$ in Fig. 4, resulting in the following relationship,

$$I_{(1-2s)f0} = I_{r,(1-2s)f} \tag{8}$$

where $I_{(1-2s)f0}$ is the stator current harmonic at the frequency of $(1-2s)\cdot f_0$.

B. Motor Impedances

The total impedance of a motor with rotor cage fault, while neglecting magnetizing reactance and the stator resistance, is

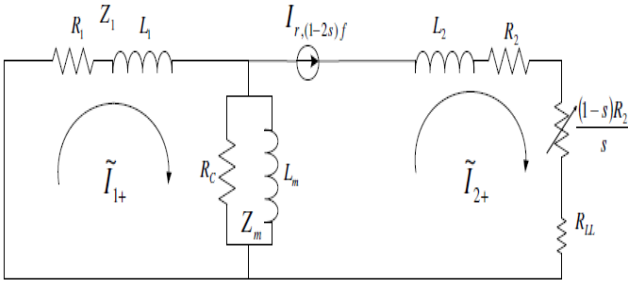

Fig. 4. Motor equivalent circuit at $(1-2s)\cdot f_0$.

$$Z_{(1-2s)f_0} = -\frac{R_2}{s} + j\omega_0(1-2s)L_{lk}. \tag{9}$$

$$Z_{(1+2s)f_0} = \frac{R_2}{3s} + j\omega_0(1+2s)L_{lk} \tag{10}$$

where R_2 is the rotor resistance, and L_{lk} is the total stator and rotor leakage inductance.

Following the same assumption as in (9) and (10), the total impedance of the same motor at the fundamental frequency f_0 is

$$Z_{f_0} = \frac{R_2}{s} + j\omega_0 L_{lk} = |Z_{f_0}|(\cos\phi + j\sin\phi) \tag{11}$$

where φ is the power angle at the fundamental frequency.

Using the same notion as in (11), equations (9) and (10) can be simplified to

$$Z_{(1-2s)f_0} = |Z_{f_0}|(-\cos\phi + j\sin\phi). \tag{12}$$

$$Z_{(1+2s)f_0} = |Z_{f_0}|(\tfrac{1}{3}\cos\phi + j\sin\phi) \tag{13}$$

C. Correlations Among Fault Signature Currents

According to Fig. 3, the left- and right-sideband currents $I_{(1-2s)f0}$ and $I_{(1+2s)f0}$, located at $(1-2s)\cdot f_0$ and $(1+2s)\cdot f_0$, respectively, are two most dominant fault signature currents. The left-sideband current $I_{(1-2s)f0}$ is proportional to the ratio of the negative sequence flux Ψ_n to the motor impedance $Z_{(1-2s)f0}$, while the right-sideband current $I_{(1+2s)f0}$ is proportional to the ratio of the positive sequence flux Ψ_p to the motor impedance $Z_{(1+2s)f0}$. Consequently, the following relationship is established

$$I_{(1-2s)f_0} = -\left(I_{(1+2s)f_0} Z_{(1+2s)f_0}\right) \Big/ Z_{(1-2s)f_0} \tag{14}$$

Note that the minus sign in (14) is caused by difference in the signs between the positive and negative sequence fluxes.

Substituting (12) and (13) to (14) yields

$$I_{(1-2s)f_0} = I_{(1+2s)f_0} \frac{(\tfrac{1}{3}\cos\phi + j\sin\phi)}{(\cos\phi - j\sin\phi)} \tag{15}$$

Note that $\cos\varphi - j\cdot\sin\varphi = \exp(-j\varphi)$, equation (15) is further simplified to

$$I_{(1-2s)f_0} = I_{(1+2s)f_0} \cdot (\tfrac{1}{3}\cos\phi + j\sin\phi)\cdot\exp(j\phi) \tag{16}$$

D. Fault Severity Index

Given the proportional relationship between the sideband current harmonics and fluxes in Section III. C. , equation (7) is transformed to

$$\frac{\left|I_{(1-2s)f_0}\right|}{\left|I_{r,f_0}\right|} \approx \frac{1}{N} \qquad (17)$$

where $I_{r,f0}$ is the rotor current at the fundamental frequency. In (17), the number of rotor bars N is assumed to be sufficiently large so that $1/(N-1)$ can be approximated by $1/N$.

Based on (17), the fault severity is evaluated using the overall left-sideband current and the fundamental component of the stator current [18]

$$\frac{\left|I_{(1-2s)f_0} + \left|I_{(1+2s)f_0}\right| \cdot \left|\tfrac{1}{3}\cos\phi + j\sin\phi\right| \cdot \exp(j\phi)\right|}{\left|I_{s,f_0} - I_{s_0,f_0}\exp j(\phi - 90^\circ)\right|} \approx \frac{1}{N} \qquad (18)$$

where numerator is the combined overall left-sideband current, and the denominator is the rotor current at the fundamental frequency, which is equivalent to the stator current at the fundament frequency minus a phase-shifted stator current $I_{s0,f0}$ that is measured at no load operating condition.

A normalized version of the fault severity is calculated by multiplying the left side of (18) with the number of rotor bars N [18]

$$FSI = \frac{\left|I_{(1-2s)f_0} + \left|I_{(1+2s)f_0}\right| \cdot \left|\tfrac{1}{3}\cos\phi + j\sin\phi\right| \cdot \exp(j\phi)\right|}{\left|I_{s,f_0} - I_{s_0,f_0}\exp j(\phi - 90^\circ)\right|} N \qquad (19)$$

Following the calculation of (19), the fault severity index (FSI) has a value that is proportional to the number of broken bars in the rotor cage. When the motor is under heavy load, the fault severity index is further simplified to [18]

$$FSI = \frac{\left|I_{(1-2s)f_0} + \left|I_{(1+2s)f_0}\right| \cdot \exp(j\phi)\right|}{\left|I_{s,f_0} - I_{s_0,f_0}\exp j(\phi - 90^\circ)\right|} N . \qquad (20)$$

Based on the fault severity index (19) and (20), a rotor cage fault detection scheme is outlined in Fig. 5.

The stator phase current and line-to-line voltage signals are measured using current and voltage sensors. The power factor is then calculated at steady-state motor operation using measured voltages and currents. The spectrum of the stator current is then obtained with the magnitudes of all stator current at known frequencies in (19) and (20). The fault severity of the rotor cage fault is then evaluated.

Based on the evaluated fault severity, a decision-making system can then decide whether a rotor bar breakage exists. The threshold can be determined based on the nameplate information of an induction motor. If a fault is detected, a warning is issued to allow the user to schedule maintenance or repair actions.

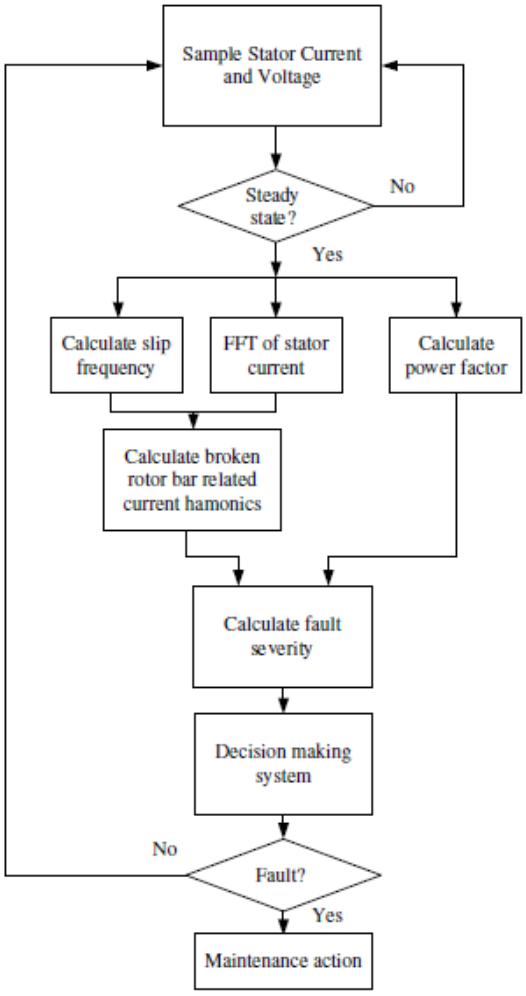

Fig. 5. Fault-severity-index-based rotor cage fault detection scheme.

IV. Broken Rotor Bar Detection – Practical Considerations

The fault severity index (19) or (20) is calculated from motor terminal voltage and current measurements. The use of only voltage and current measurements allows for non-intrusive and cost-efficient implementation. In practice, the voltage and current measurements are often fraught with interferences and noise. Therefore, advanced digital signal post-processing is an essential element in digital signal processing. In addition, successful detection of rotor cage fault is also dependent on the detection scheme's ability to predict rotor cage failure without resorting to any baseline data for comparative analysis.

To address the issue of reliable broken rotor bar detection with minimal false positives, the decision making system has to incorporate certain flexibility to handle various motors with vastly different operating conditions. A fuzzy system has been experimentally tested for reliable decision-making in the detection or rotor cage failures. The result shows that the fuzzy system can help increase the reliability of the

overall rotor cage fault detection.

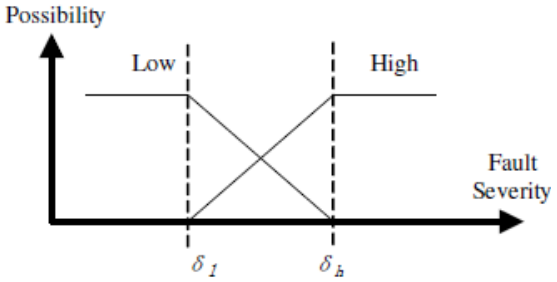

Fig. 6. Membership function of fuzzy system.

A. Noise Reduction via Filtering

Given a fault severity index FSI_n calculated as step n, a filter in the form of (21) is applied to produce a filtered fault severity index FSI'_n

$$FSI'_n = \frac{P_{n-1}+Q}{P_{n-1}+Q+0.01}\cdot FSI_n + \frac{0.01}{P_{n-1}+Q+0.01}FSI'_{n-1}. \quad (21)$$

In (21), the coefficient P_n is defined as

$$P_n = \begin{cases} 0.1, & \text{if } \left|FSI_n - FSI_{n-1}\right| > 0.05, \\ \dfrac{0.01\cdot P_{n-1}}{P_{n-1}+Q+0.01}, & \text{otherwise.} \end{cases} \quad (22)$$

with initial values FSI'_0=FSI'_0 and P_0=0.01.

B. Decision Making via Fuzzy System

The robustness of fuzzy systems can help increase the reliability of the overall rotor cage fault detection. A commonly used membership function is given in Fig. 6. In this figure, a lower fault severity index indicates that the machine is healthy; while a higher fault severity index predicts failure of an induction motor.

In Fig. 6, the region below δ_l represents a healthy induction machine (i.e., no presence of rotor fault or failure). When the fault severity indices fall into this region, there is a 100% confidence level of indicating a healthy motor condition. The region above δ_h is defined to include fault severity indices that indicate a 100% confidence level in an faulty rotor condition.

In Fig. 6, the region between δ_l and δ_h represents a zone wherein each fault severity value has a corresponding low fault possibility, indicating a confidence level for a determination that the motor is healthy, and a corresponding high fault possibility, indicating a confidence level for a determination that that the motor is unhealthy.

To account for intrinsic rotor unbalance, which tends to be larger for smaller motors, and remains relatively stable for large medium-voltage motors, the threshold δ_l is defined by

$$\delta_l = \frac{25}{500+Hp} + 0.05. \quad (23)$$

where Hp is the motor's rated horsepower.

In an ideal condition, one broken rotor bar is associated with a threshold of δ_h=1. In practice, however, the non-idealities of the motor, such as the magnetic saturation, end-

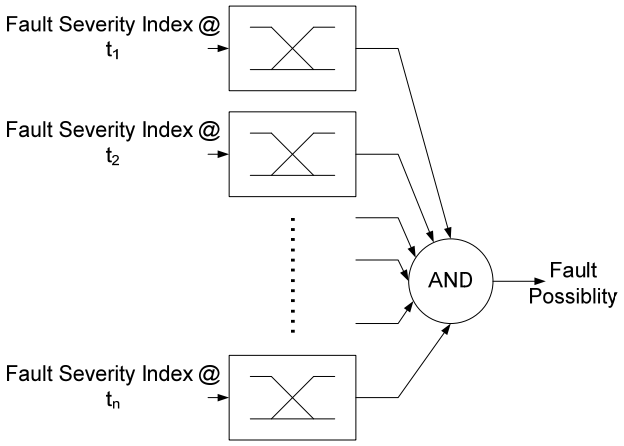

Fig. 7. Multiple fault severity indices combined to predict fault possibility.

ring resistances and inductances, cause the fault severity index to be less than 1 when only one rotor bar is broken. To accommodate the motor's non-idealities, the following formula is used

$$\delta_h = \min\left(\delta_l + 0.2,\ \frac{3.5\pi p^2 L}{ND+10\pi p^2 L}\right). \quad (24)$$

where p is the number of pole pairs; N is the total number of rotor bars; D is the diameter of the rotor cage; L is the length of the rotor cage. In practice, when the actual diameter of the rotor cage is not readily available, the quantity D can be substituted with the diameter of the stator frame. Similarly, the quantity L can be substituted with the length of the stator frame.

To further improve the reliability of the rotor cage failure detection, multiple fault severity indices acquired at different instants are combined to improve the detection accuracy as shown in Fig. 7 below.

In Fig. 7, the "AND" operation is implemented via

$$\text{AND} \equiv \min\left[FSI'(t_1),\ FSI'(t_2),\ \cdots,\ FSI'(t_n)\right]. \quad (25)$$

In practice, the number of inputs used in (25) may be adjusted depending on the requirements of practical applications. A large number is usually associated with improved reliability, while a small number is usually associated with faster response. The recommended number of inputs is between 3 and 7.

To summarize, given the motor's horsepower, its number of pole pairs, number of the rotor bars, rotor's diameter and rotor's length, the detection scheme is able to provide useful information regarding motor's cage rotor status.

In addition, because the motor does not always operate at steady-state conditions, and because the rotor bar failure develops rather slowly over the time, it is not necessary to continuously monitor the motor terminal voltages and

currents. A suggested monitoring interval is about once every hour. For motors driving critical processes, this

(a)

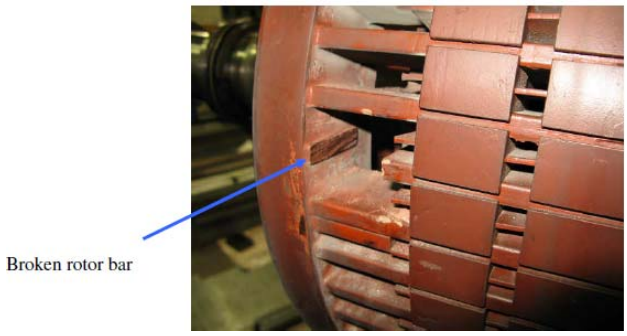

(b)

Fig. 8. Medium-voltage induction motor with one broken rotor bar. (a) The medium-voltage test motor. (b) The rotor cage with one rotor bar removed.

monitoring interval can be changed to as fast as once every 120 seconds when appropriate. This helps safeguard the motor against potential failures on its rotor cage.

V. Experimental Results

To test the reliability of the fault severity evaluation algorithm on large medium-voltage motors, a 500-hp 4.16kV induction motor is tested under both healthy and faulty conditions. Experimental setup and test results are reported in this section.

A. Medium-Voltage Induction Motor Test Setup

The nameplate information of the medium-voltage induction motor is shown in Table I.

TABLE I
MEDIUM-VOLTAGE INDUCTION MOTOR NAMEPLATE DATA

HP	500
Rated Frequency (Hz)	60
Rated Voltage (V)	4160
Full Load Current (A)	78
Speed (r/min)	888
Service Factor	1.15

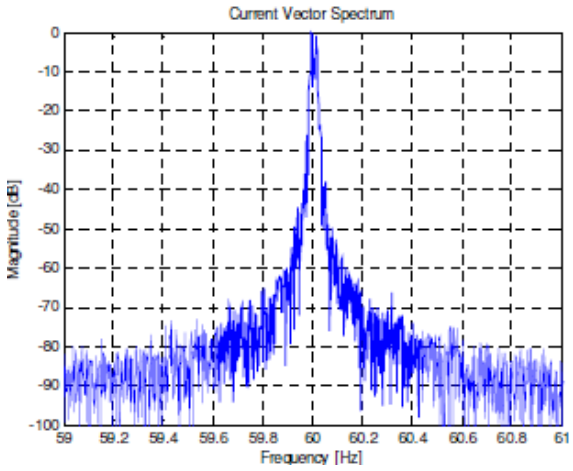

(a)

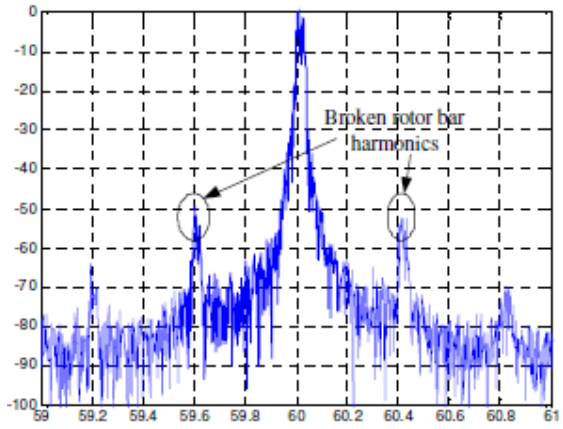

(b)

Fig. 9. Stator current spectrum. (a) Healthy motor. (b) Motor with one broken bar.

To emulate a broken rotor bar failure, a small part of the rotor bar is completely removed. To avoid the subsequent mechanical unbalance and resultant torque pulsation, the rotor bar is then glued to a close rotor bar. Fig. 8 shows the field photos of the medium-voltage motor with the created one broken rotor bar failure.

B. Experimental Results

Fig. 9 shows the stator current spectra of the medium-voltage motor under healthy and faulty condition. The motor is running at 75% of its rated load. The broken rotor bar related harmonics, as marked on Fig. 9 in the neighborhood of 59.4 and 60.4 Hz, are recorded and passed to the block that calculates the fault severity (Fig. 5).

Similar experiments have also been performed on the same motor when running at 50% and 100% of its rated load. The fault severity indices calculated from the broken rotor bar related harmonics at those load levels are plotted in Fig. 10(a).

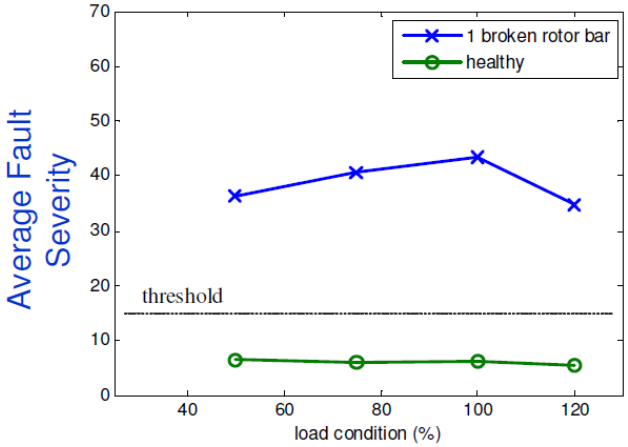

(a)

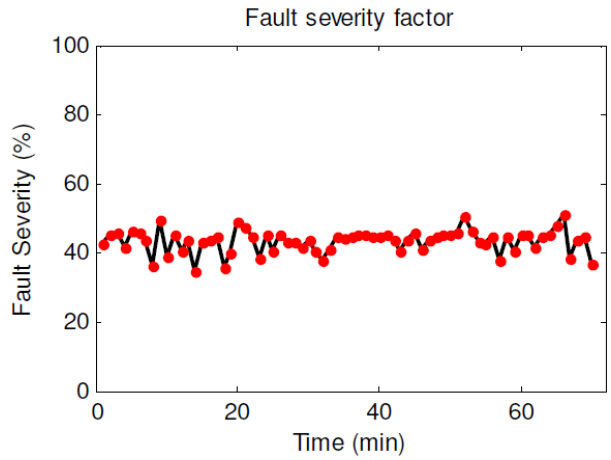

(b)

Fig. 10. Fault severity index. (a) Calculated from healthy and faulty motors with various load levels. (b) Calculated from different data sets.

To further evaluate the reliability of the proposed fault severity index, a total of 70 data sets are collected from the test motor with one broken rotor bar fault. Each data set is sampled at 8 kHz for 10 seconds. The corresponding fault severity indices are calculated based on those sampled voltages and currents and plotted in Fig. 10(b). It can be observed from Fig. 10(b) that the calculated fault severity index is almost constant from different data sets. This guarantees the reliability of the fault detection when the proposed fault severity index is used.

Fig. 11(a) shows the stator current spectrum of the test motor with different rotor cage conditions. It is worth noting that the rotor cage condition with 2 broken rotor bar condition is created on the test motor in the same way as the condition with 1 broken rotor bar. All tests are performed at 50% of the motor's rated load condition. Therefore, the stator's current at 60 Hz is held at roughly the same value in all 3 cases.

As can be seen from Fig. 11(a), starting from no broken bar fault to 2-broken bar fault, both the left and right sidebands at 60±0.28 Hz, as specified in (1), become progressively larger as the rotor cage condition deteriorates.

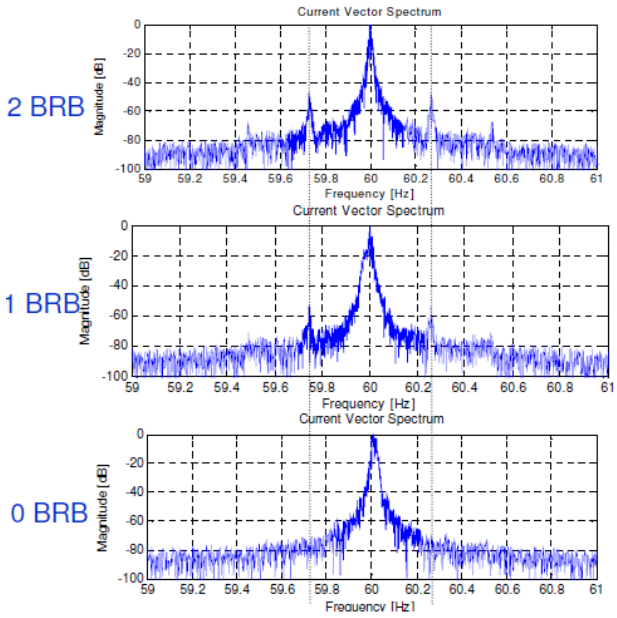

(a)

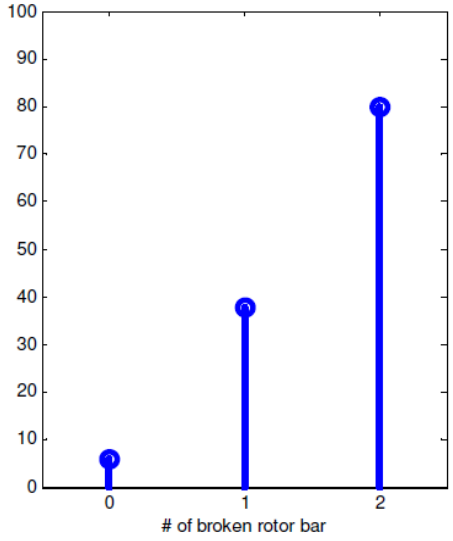

(b)

Fig. 11. Rotor cage fault detection under various rotor cage conditions. (a) Stator current spectra. (b) Fault severity indices.

For an ideal motor, the fault severity index at 2 broken rotor bars is expected be twice the index for the same motor with only one broken rotor bar. In practice, this is not always the case due to the inherent noise and interference from the stator current spectrum, plus the fact that the motor may not operate at a perfect steady-state condition each time the voltages and currents are sampled.

Fig. 11(b) shows the fault severity indices calculated from the sample voltages and currents under different rotor cage conditions. It is apparent that the fault severity index becomes progressively larger as the number of broken rotor bars increases. For the rotor cage fault conditions with 1

and 2 broken bars, the ratio of the fault severity index to the number broken rotor bars is held at close to 40%. This rotor-cage-fault-condition-independent ratio hence proves that the proposed fault severity index servers as a good indicator of the rotor cage condition.

C. *Implementation in Protective Relays*

The aforementioned broken rotor bar detection algorithm has been implemented in a series of motor protective relays. The motor protective relays also implement many other protection, metering, monitoring, control and communication features. For example, the motor protective relays provide phase instantaneous overcurrent protection (50P), phase inverse-time overcurrent protection (51P), thermal protection (49), locked rotor protection (49S/51), jam or stall protection (50J), and temperature protection with optional UTRD (49/38).

The added diagnostic feature on broken rotor bar detection brings non-invasive on-line predictive diagnostics to critical processes in many process industries. This feature, in conjunction with other condition monitoring and predictive diagnostics techniques, such as the pump cavitation or loss of vacuum detection, allows plant managers to schedule motors maintenance in a timely fashion, and hence avoids expensive financial cost, especially associated with the loss of production in a process downtime situation due to motor failures in critical applications [5], [9].

Fig. 12(a) shows the faceplate of a protective relay with broken rotor bar (BRB) detection settings displayed on its LCD panel. The settings shown on the relay's faceplate include a motor's horse power, its number of pole-pairs, rotor bars, rotor diameter and rotor length.

The above settings are also accessible through a relay setting software running on a personal computer. Fig. 12(b) shows a screenshot of the protective relay set-up for the broken rotor bar algorithm where motor design parameters such as horsepower, number of poles, number of rotor bars, rotor diameter and rotor length are entered. The broken rotor bar detection settings are shown on the right column in Fig. 12(b). These settings serve as inputs to the algorithm. Once the settings are configured and confirmed in the software, they are transferred through a communication link to the protective relay for monitoring and protection.

The broken rotor bar detection algorithm analyzes stator current spectra via Fourier transform techniques. Two Fourier transform techniques have been considered in the protective relays. The first one uses a standard fast Fourier transform (FFT), while the second one implements an enhanced version of FFT that provides better accuracy with the tradeoff being additional signal processing time. Stable current signal conditions and near full load current are required. The algorithm will process data when these stable conditions are met.

If a broken rotor bar condition is detected, an "alarm" output is generated and communicated, either via an on-bard relay contact or via a network. Depending on operating conditions, at times the relay may be unable to perform a

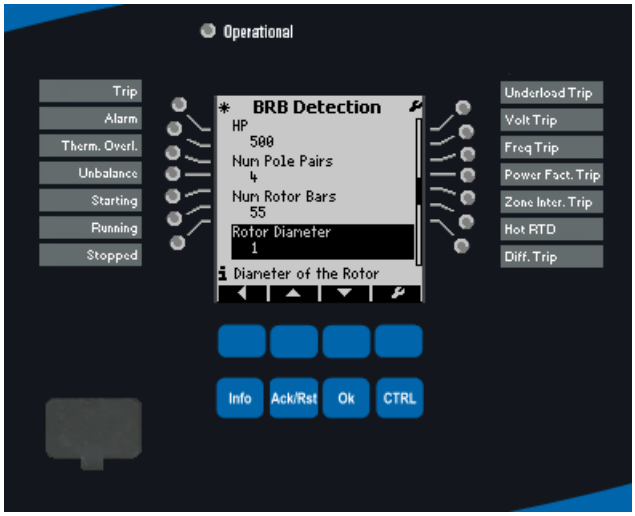

(a)

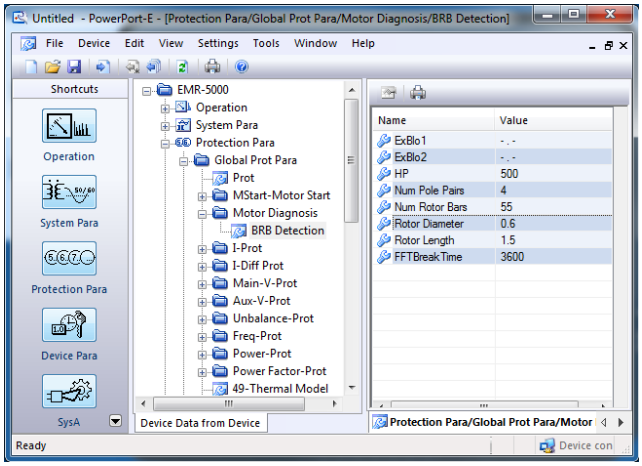

(b)

Fig. 12. Broken rotor bar detection in protective relay. (a) Faceplate of a protective relay with broken rotor bar detection setting page. (b) Software screenshot with broken rotor bar detection setting page.

reliable broken rotor bar analysis. This is typically due to conditions including:

- The supply frequency is more than 0.1 Hz away from the nominal frequency.
- Invalid data, such as two consecutive zeros.
- The motor is not running at steady-state condition.
- The frequency is not stable.
- The motor is operating at less than 85% of its full load.

Generally speaking, a rotor bar failure develops slowly, and hence there is no need to monitor the rotor bar status all the time. In practice, the protective relay performs broken rotor bar detection at an interval specified by a setting called "FFTBreak Time." The default setting is 3600 seconds, i.e., the protective relays performs a broken rotor bar detection once every hour. According to Table II, this setting can be adjusted anywhere between 120 and 60000 seconds. Table II lists detailed setting parameters, their ranges of and default

values.

TABLE II
PROTECTION PARAMETERS

Parameter	Description	Range	Default
HP	Horse Power	1 - 500000	500
Num Pole Pairs	Number of pole pairs of the motor	1-16	4
Num Rotor Bars	Number of rotor bars	10 – 5000	55
Rotor Diameter	Diameter of the rotor (in meters)	0.1 – 10	0.6
Rotor Length	The length of the rotor (in meters)	0.1 – 10	1.5
FFTBreak Time	Time between 2 FFT cycles (in seconds)	120 – 60000	3600

In process industry applications, many medium-voltage motors are also driven by variable frequency drives (VFDs). For those VFD-driven motors in rolling mills and other applications, the fast changing VFD output frequencies and interferences from drive switching transients pose potential challenges to the broken rotor bar detection algorithm, and further testing is necessary to confirm the broken rotor bar detection's performance in such environment. In addition to that, another possible solution, for VFD driven motor loads, is to utilize the VFD output to generate voltage pulses in order to excite the motor's stator winding at zero speed [19], and then detect changes in spatial distribution of the transient inductance caused by broken rotor bars.

VI. CONCLUSIONS

To improve process reliability in critical motor applications, new on-line predictive diagnostic tools for broken rotor bar detection on large AC motors are needed and available. Application of a new innovative algorithm using a fault severity evaluation technique offers improvements over legacy broken rotor bar detection systems, which rely primarily on the monitoring of changes in the stator current spectra. The new approach includes a fault severity index which calculates a ratio of broken-rotor-bar-induced stator current harmonics to the rotor current. This ratio has been experimentally demonstrated to be independent of the motor operating conditions. Experimental results also confirm that the fault severity index guarantees reliable detection of rotor cage fault in practical applications in the absence of baseline data on rotor cage conditions. A decision-making system is proposed to warn the user for any rotor cage failures based on the proposed fault severity analysis technique. All parameters required in this technique, including motor nameplate data and motor sizes can be programmed in commercially available motor protective relays. The diagnostic notification of impending rotor failures brings an added dimension of protection to motors serving critical process loads in motor wellness monitoring and predictive maintenance programs, rendering comprehensive protections of industry's largest and most expensive motors against both conventional faults and potential broken rotor bar faults.

ACKNOWLEDGMENT

The authors would like to acknowledge P. Zhang and T. G. Habetler for their major contributions to the development and validation of this work.

REFERENCES

[1] L. H. Dreinhoefer and F. D. Magee, "AC drives in the metals industry," in *Conf. Rec. IEEE IAS Annual Meeting*, Pittsburgh, PA, Oct. 13-18, 2002, vol. 2, pp. 1234-1239.

[2] B. Dick, "Spotting drives for large motors," in *Conf. Rec. IEEE-IAS/PCA Cement Industry Technical Conference*, Jacksonville, FL, May 5 -9, 2002, pp. 77-83.

[3] W. J. Jackson, "Mill motors for adjustable-speed AC drives," *IEEE Trans. Ind. Appl.*, vol. 29, no. 3, pp. 566-572, May/Jun. 1993.

[4] A. K. Chattopadhyay, "Alternating current drives in the steel industry," IEEE Ind. Electron. Mag., vol. 4, no. 4, pp. 30-42, Dec. 2010.

[5] B. Lu, D. Durocher, and P. Stemper, "Predictive maintenance techniques," *IEEE Ind. Appl. Mag.*, vol. 15, no. 6, pp. 52-60, Nov./Dec. 2009.

[6] IEEE Committee Report, "Report of large motor reliability survey of industrial and commercial installations, Part I," *IEEE Trans. Ind. Appl.*, vol. IA-21, no. 4, pp. 853-864, Jul./Aug. 1985.

[7] IEEE Committee Report, "Report of large motor reliability survey of industrial and commercial installations, Part II," *IEEE Trans. Ind. Appl.*, vol. IA-21, no. 4, pp. 865-872, Jul./Aug. 1985.

[8] A. H. Bonnett and G. C. Soukup, "Cause and analysis of stator and rotor failures in three-phase squirrel-cage induction motors," *IEEE Trans. Ind. Appl.*, vol. 28, no. 4, pp. 921-937, Jul./Aug. 1992.

[9] D. B. Durocher and G. R. Feldmeier, "Future control technologies in motor diagnostics and system wellness," in *Conf. Rec. IEEE IAS Pulp & Paper Ind. Tech. Conf.*, Charleston, SC, Jun. 16-20, 2003, pp. 98-106.

[10] A. H. Bonnett and C. Yung, "Increased efficiency versus increased reliability," *IEEE Ind. Appl. Mag.*, vol. 14, no. 1, pp. 29-36, Jan./Feb. 2008.

[11] O. V. Thorsen and M. Dalva, "Failure identification and analysis for high-voltage induction motors in the petrochemical industry," *IEEE Trans. Ind. Appl.*, vol. 35, no. 4, pp. 810-818, Jul./Aug. 1999.

[12] M. F. Cabanas, et al., "Analysis of the fatigue causes on the rotor bars of squirrel cage asynchronous motors: experimental analysis and modelling of medium voltage motors," in *Diagnostics for Electric Machines, Power Electronics and Drives, 2003. SDEMPED 2003. 4th IEEE International Symposium on*, 2003, pp. 247-252.

[13] A. H. Bonnett and G. C. Soukup, "Analysis of rotor failures in squirrel-cage induction motors," *IEEE Trans. Ind. Appl.*, vol. 24, no. 6, pp. 1124-1130, Nov./Dec. 1988.

[14] S. Nandi, H. A. Toliyat, and X. Li, "Condition monitoring and fault diagnosis of electrical motors - A review," *IEEE Trans. Energy Convers.*, vol. 20, no. 4, pp. 719-729, Dec. 2005.

[15] G. B. Kliman, R. A. Koegl, J. Stein, R. D. Endicott, and M. W. Madden,, "Noninvasive detection of broken rotor bars in operating induction motors," *IEEE Trans. Energy Convers.*, vol. 3, no. 4, pp. 873-879.

[16] N. M. Elkasabgy, A. R. Eastham, and G. E. Dawson, , "Detection of broken bars in the cage rotor on an induction machine," *IEEE Trans. Ind. Appl.*, vol. 28, no. 1, pp. 165-171, Jan./Feb. 1992.

[17] F. Filippetti, G. Franceschini, C. Tassoni, and P. Vas, "AI techniques in induction machines diagnosis including the speed ripple effect," *IEEE Trans. Ind. Appl.*, vol. 34, no. 1, pp. 98-108, Jan./Feb. 1998.

[18] P. Zhang, B. Lu, and T. Habetler, "System and method for detecting fault in an AC machine," U.S. Patent 8,405,339, Mar. 26, 2013.

[19] T. M. Wolbank, G. Stojicic and P. Nussbaumer, "Monitoring of partially broken rotor bars in induction machine drives," in *Conf. Rec. 36th IEEE Industrial Electronics Society Annual Conference*, Glendale, AZ, Nov. 7-10, 2010, pp. 912-917.